

# Combined Scanning Force Microscopy and Electrochemical Quartz Microbalance *in-Situ* Investigation of Specific Adsorption and Phase Change Processes at the Silver/Halogenide Interface

Wolfgang Kautek,\* Sabine Dieluweit,<sup>†</sup> and Mario Sahre

Laboratory for Thin Film Technology, Federal Institute for Materials Research and Testing,  
D-12200 Berlin, Germany

Received: September 6, 1996; In Final Form: December 4, 1996<sup>⊗</sup>

Specific adsorption of halogenides and silver halogenide phase formation was investigated by the combination of electrochemical quartz microbalance measurements (EQMB), topographical *in-situ* scanning force microscopy (SFM), and *in-situ* lateral force microscopy (LFM). *In-situ* LFM can be employed to monitor specific adsorption and, more generally, chemical conversion reactions in submonolayers of atomic species which are inaccessible to topological imaging by SFM. Reorganization of the electrochemical double layer during specific adsorption caused nanotribological changes. Hydrated anions in the outer Helmholtz plain are not locally bonded to a specific site and give low LFM friction values. Specifically adsorbed anions and ion pairs, on the other hand, impede the lateral cantilever translation, resulting in increased friction. EQMB measurements yielded data corresponding to the formation of up to one monolayer of specifically adsorbed cation–halogenide ion pairs. Anodic dissolution of silver to  $\text{AgO}^-$  and the formation of  $\text{Ag}_2\text{O}$  islands in a halogenide-free alkaline solution contributed to a roughening of the surface. Long range *in-situ* SFM showed that silver halogenide phases are anodically nonuniformly formed as smooth islands located in no observable correspondence to grain surfaces or boundaries suggesting a dissolution–precipitation growth mechanism.  $\text{AgI}$  and  $\text{AgBr}$  phases can almost reversibly be reduced. Irreversible mass gains after an oxidation–reduction cycle can be associated with  $\text{Ag}$  deposition near surface steps from soluble  $\text{AgI}_{n+1}^{n-}$  and  $\text{AgBr}_{n+1}^{n-}$  species which were dissolved into the electrolyte bulk during previous anodic scans in the dissolution potential range. In the presence of chloride, the silver surface is vigorously electropolished and soluble  $\text{AgCl}_{n+1}^{n-}$  species evolve, while  $\text{AgCl}$  islands precipitate on the newly generated surface regardless of the original silver grain topography.

## 1. Introduction

Modern micromechanical and microelectronic devices exhibit features which are continuously miniaturized down into the nanometer range. Surface properties and chemical reactivity tend to dominate the dimensional and physical properties. Thermodynamic bulk properties of the solids employed compete with physicochemical surface properties. The geometrical stability of electronically conductive structures, like, e.g., leads, contacts, capacitor electrodes, and gates, is the prerequisite of the functional reliability of the respective devices. Environmental chemical factors, reactive gases (e.g., air) and/or fluids (e.g., condensates), open reaction channels for chemical conversion and/or corrosion. Protective packaging materials can degrade or themselves may react with the active microstructures.

Polycrystalline silver is widely applied in microstructures. It is less inert than gold. Reactive anions like certain halogenides may form local chemical bonds with silver surface atoms. These specifically adsorbed species, therefore, show a higher surface excess than can be explained by simple electrostatic interaction. This accumulation could be quantified *in-situ* by electrochemical capacitance,<sup>1,2</sup> electrochemical quartz microbalance (EQMB) measurements,<sup>3</sup> and *ex-situ* by photoelectron spectroscopy.<sup>4</sup> Some indirect evidence for specific adsorption of chloride could be attributed to blurring of scanning

force microscopy (SFM) images at positively charged  $\text{Ag}$  single crystals in chloride.<sup>5</sup> This was explained by the increased mobility of surface  $\text{Ag}$  atoms while chloride is adsorbed.

Silver halogenide phase formation takes place on anodized silver surfaces. Such  $\text{Ag}/\text{Ag}$ -halogenide composite surfaces play an important technological role as reference electrodes in many electroanalytical and medical applications (e.g., electrocardiogram electrodes). Electrochemical oxidation reduction cycles (ORC's) in the presence of halogenides were extensively used to roughen and condition silver electrodes for surface enhanced Raman spectroscopy (SERS) investigations.<sup>6</sup>

Quartz microbalance devices have been used in contact with liquids to monitor mass<sup>7–11</sup> and viscosity changes at gold electrode surfaces.<sup>12–14</sup> The resonant frequency change  $\Delta f$  of the shear vibration of a quartz crystal with the piezoelectrically active area  $A$  characterized by a shear modulus  $\mu_Q$ , a density  $\rho_Q$ , and the resonant frequency  $f_0$  in contact with a liquid of density  $\rho_L$  and viscosity  $\eta_L$  is affected not only by rigid mass changes  $\Delta m$  but also by viscosity changes  $\Delta((\eta_L \rho_L)^{1/2})$  in the interface:<sup>7</sup>

$$\Delta f = - \frac{2f_0^2}{(\rho_Q \mu_Q)^{1/2}} \left[ \frac{\Delta m}{A} + \frac{\Delta((\eta_L \rho_L)^{1/2})}{(4\pi f_0)^{1/2}} \right] \quad (1)$$

Assuming a no-slip boundary condition, i.e., a transversal velocity of the metal electrode film surface equal to the adjacent liquid layer, a viscous penetration depth is proportional to the viscosity, since liquid films show no elasticity. The mass of this liquid layer causes the vibrating mass to increase and the

\* Corresponding author.

<sup>†</sup> Present address: Center for Ultrastructure Research, Vienna University of Agriculture, Forestry and Renewable Natural Resources, Gregor-Mendel-Strasse 33, A-1180 Vienna, Austria.

<sup>⊗</sup> Abstract published in *Advance ACS Abstracts*, March 1, 1997.

resonant frequency to decrease. A further complication in the interpretation of a quartz balance frequency change is the surface roughness. Trapping of liquid in surface cavities can result in an additional mass component depending on the amount of trapped liquid and the size of the cavities.<sup>15–17</sup> Roughness change effects in the oxide monolayer region of gold, e.g., could be ruled out by *ex-situ* scanning tunneling microscopic (STM) roughness statistical investigations.<sup>18</sup>

Nanotribological investigations demonstrated that interaction between certain liquids and solids results in so-called boundary effects, i.e., higher molecular order and viscosity in the first six solvent molecule layers at variance to the liquid bulk.<sup>19</sup> However, there are no values for the interfacial viscosity because of the lack of knowledge of the interfacial structures. It was suggested that the small polar water molecules formed ordered packed structures at the solid–liquid interface due to oriented dipoles. Molecular dynamics simulations without consideration of potential changes suggested that water adopts an ordered structure similar to ice over a thickness of about 1 nm on platinum.<sup>20</sup> *In-situ* far-infrared studies of silver suggested that water is bound via oxygen irrespectively of the electrode charging state.<sup>21</sup> Synchrotron X-ray scattering investigations showed that water is oriented in layers extending about three molecular diameters from the electrode, with the oxygen up positive of the point of zero charge (pzc). Positive charging resulted in a substantial compression in the first dipole layer because the surface density increased from  $1.15 \times 10^{15} \text{ cm}^{-2}$ , at the pzc, to  $2.6 \times 10^{15} \text{ cm}^{-2}$ ,  $\sim 0.5 \text{ V}$  positive of the pzc.<sup>22</sup> More investigations of that kind are necessary to clarify this model. Structural reorganizations of electrolyte molecules adjacent, e.g., to a gold electrode in the potential range from the hydrogen evolution up to the bulk oxide formation including the OH-monolayer formation do not have to be generally invoked to explain the observed frequency data.<sup>11</sup> In this respect, electrochemical charge and EQMB frequency measurements led to unexplainable discrepancies between anodic and cathodic charge and mass changes on silver.<sup>3</sup>

We therefore undertook a long-range topological *in-situ* scanning force microscopy (SFM) and *in-situ* lateral force microscopy (LFM) investigation of silver on an electrochemical quartz microbalance (EQMB). Scanning probe microscopy (SPM) like scanning tunneling (STM) and scanning force microscopy (SFM) exhibits a promising potential for metrology not only in the atomic but even more in the nanometer scale range,<sup>23,24</sup> which is of practical relevance to technological applications in micro- and nanotechnology. Practical environments have been simulated by aqueous electrolytes containing inert or reactive components ubiquitous in technical conditions, which are hydroxide and halogenide ions.<sup>25</sup> Recently, morphological conversions like, e.g., roughness changes due to electrochemical anodic treatment were studied by emersion procedures: an EQMB gold electrode was first submitted to the reactive medium and then withdrawn and introduced into an *ex-situ* STM system.<sup>18</sup> This method suffered from that particular surface regions could not be repeatedly addressed and imaged. Thus, only statistical evaluations were possible. *In-situ* SFM systems, on the other hand, allow topological analyses during the electrochemical control of the substrate potential and the workfunction, respectively, so that chemical surface reactions can be monitored at the same time.<sup>26</sup> It will be shown that the combination of these true *in-situ* techniques, SFM, LFM, and EQMB, providing electrical charge, mass, morphology, and nanotribological data, can contribute valuable information in the resolution of fundamentally and technologically interesting reactive interfacial systems.

## 2. Experimental Section

Polycrystalline silver films with a chromium flush ( $\sim 1.5 \text{ nm}$ ) as contact mediator on optically polished 5-MHz quartz oscillator crystals (KVG, Neckarbischofsheim, Germany) served as electrode material ( $0.28 \text{ cm}^2$  area on both sides). Topographical SFM images revealed silver grain sizes of 100–200 nm. Electrolytes were prepared with analytical grade chemicals and bidistilled water. Purified (99.9999%) and water-saturated nitrogen served for deaeration. The base electrolyte consisted of 0.1 M KF and 0.01 M NaOH.

An electrochemical cell was integrated into the SFM system (Topometrix, Model Discoverer). The working electrode was positioned on a steel base plate and was contacted by means of a silver foil. As counter electrode served a Pt wire and as reference a Ag wire. Potentials have been converted to the scale of the saturated mercury sulfate electrode (MSE) used in the EQMB measurements (see below). A Latex membrane served as electrolyte containment. The top was tightly closed with a quartz window. Underneath, in the electrolyte, the cantilever was suspended and could be optically addressed by the probe laser beam through the top window. The scanner was a tripod type ( $24 \mu\text{m}$ ). Scan ranges were up to  $5 \times 5 \mu\text{m}^2$  with a resolution of  $300 \times 300$  pixels. Cantilevers used had a force constant of  $0.032 \text{ N m}^{-1}$  with two  $200\text{-}\mu\text{m}$ -long,  $18\text{-}\mu\text{m}$ -wide, and  $0.4\text{-}\mu\text{m}$ -thick v-shaped beams. The beam including the tip (radius 50 nm) consisted of  $\text{Si}_3\text{N}_4$ . The top side was coated with 30 nm Au as a laser mirror. Topography SFM imaging and LFM were run at constant force in contact mode either by two-dimensional (2D) scans or in the 1D mode where the cantilever only scanned along a single line while the monitor recorded the cantilever movement with time or at various potentials in the second dimension.

The same quartz microbalance electrodes used in the SFM were introduced into a solution-tight Teflon housing. An electrically and thermally shielded nickel-coated brass box directly attached to this mounting contained the driver circuitry. Potential and current flow over the front silver coating was controlled by a potentiostat. A gold wire served as counter electrode and a saturated mercury–mercurous sulfate electrode (MSE) as reference ( $+0.66 \text{ V}$  vs standard hydrogen electrode). The temperature of the electrochemical cell system including the quartz mounting was controlled with a precision of  $\pm 0.05 \text{ K}$ . The driver electronics consisted in a phase controlled emitter-coupled series resonator.<sup>11,13,27</sup> The ratio  $\Delta m/\Delta f$  with the piezoelectrically active area  $A$  of the quartz crystal is

$$\frac{\Delta m}{\Delta f} = - \frac{k_r A (\rho_Q \eta_Q)^{1/2}}{2f_0^2} \quad (2)$$

For an active area of  $0.28 \text{ cm}^2$  used here, we calculate  $4 \text{ ng/Hz}$ . From calibration with electrolytes of various viscosity an empirical factor  $k_r \approx 1.4$  most probably due to roughness was found. With this, we derived a ratio  $\Delta m/\Delta f \approx 5.6 \text{ ng/Hz}$ .

## 3. Results and Discussion

**3.1. Double Layer Region.** Electrochemical quartz microbalance measurements at polycrystalline silver in contact with a KF electrolyte were performed to survey the double layer region positive of the point of zero charge (pzc,  $U^{q=0}$ ) and the adjacent region of anodic dissolution and oxide formation. Polycrystalline silver shows a pzc  $U^{q=0} \approx -1.3 \text{ V}_{\text{MSE}}$  at standard conditions,<sup>28–32</sup> a  $U^{q=0} \approx -1.1 \pm 0.02 \text{ V}_{\text{MSE}}$  in  $1 \text{ mM HClO}_4$ ,<sup>33</sup> and a  $U^{q=0} \approx -1.0 \text{ V}_{\text{MSE}}$  in neutral solutions.<sup>34,35</sup> The last value is practically the same which has been observed in a neutral

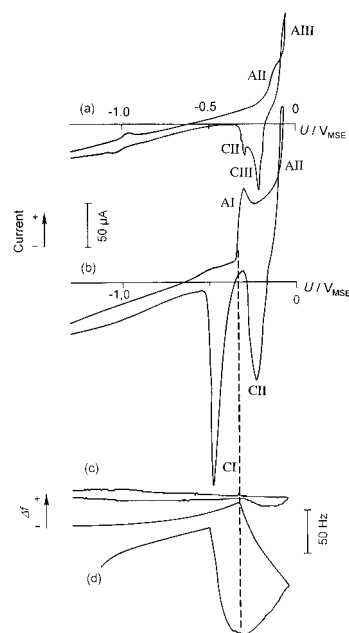


**Figure 1.** Current/frequency-potential behavior of a polycrystalline silver electrode in KF and KBr electrolyte: (a, c) 0.1 M KF, 0.01 NaOH, (b, d) 0.001 M KBr, 0.1 M KF, 0.01 NaOH.  $0.02 \text{ V s}^{-1}$ ; (c, d) quartz microbalance frequency change ( $\Delta f$ ).

KF electrolyte at monocrystalline Ag(111).<sup>36</sup> In a KF solution of pH = 12 (no specific adsorption, i.e., only anions, A, in the outer Helmholtz plain) employed in the context of the present work, the pzc is  $U_A^{q=0} \approx -0.7 \text{ V}_{\text{MSE}}$ .<sup>3,4,40</sup> Chloride, bromide, and iodide adsorb specifically in contrast to fluoride.<sup>37</sup> Therefore, KF was used as base electrolyte to study the action of hydroxide and halogenides.

Current and  $\Delta f$  of the halogenide-free case is depicted in parts a and c of Figure 1, respectively. A mass change  $\Delta m$  on the active surface area  $A$  affecting the measured frequency ( $\Delta f$ ) according to (2) consists of the contributions of cations (C) and anions (A) with hydration shells of various extents, depending on their surface density  $\Gamma$  (in  $\text{mol}/\text{cm}^2$ ), bonding state, and position in the outer (O) or inner (I) Helmholtz plane:

$$\Delta m = (\Gamma_C^O m_C^O + \Gamma_A^O m_A^O + \Gamma_X^I m_X^I + \Gamma_{CX}^I m_{CX}^I + \Delta m_\delta + \Delta m_r) A \quad (3)$$

This applies to the double layer potential region where no conversion layers are formed. Any roughness changes are considered by the term of the sum  $\Delta m_r$ . Acoustic decay layer (viscosity) changes are symbolized by  $\Delta m_\delta$ . The double layer charging current (Figure 1a) is widely masked by spurious processes like, e.g., the reduction of oxygen traces. The  $\Delta f$  trace in the positive range shows a slight mass increase mainly due to the charging of the outer Helmholtz layer with fluoride ( $\Gamma_A^O m_A^O$ ) and the inner Helmholtz layer with mainly ion pairs ( $\Gamma_{CX}^I m_{CX}^I$ ) accompanied by the repulsion of the hydrated cations ( $\Gamma_C^O m_C^O$ ).<sup>3</sup>

**3.2. Oxide Formation.** The dissolution and the oxide formation of Ag in an aqueous KF electrolyte of pH 12 occurs almost at the same electrode potential (Table 1). The cyclic voltammogram (Figure 1a) is in accordance with this thermodynamical expectation, i.e.,  $U_{\text{Ag}/\text{AgO}^-}^0 \approx -0.19 \text{ V}_{\text{MSE}}$  and  $U_{\text{Ag}/\text{Ag}_2\text{O}}^0 \approx -0.16 \text{ V}_{\text{MSE}}$ .<sup>38</sup> The anodic current peak AII indicates the formation of soluble  $\text{AgO}^-$  species, which are reduced by current CII. The  $\text{Ag}_2\text{O}$  (or  $\text{AgOH}$ ) phase formation occurs a little more positive at AIII.  $\text{Ag}_2\text{O}$  is reduced on the reverse scan at CIII. During the appearance of AII and AIII,

**TABLE 1: Peak Identification of the Cyclic Voltammograms of the Silver Halogenide Systems (e.g.,  $\text{Br}^-$  in Figure 1)**

	$\text{F}^-$	$\text{Cl}^-$	$\text{Br}^-$
AI		$\text{Ag} \rightarrow \text{AgCl}$	$\text{Ag} \rightarrow \text{AgBr}$
$U^0, \text{V}_{\text{MSE}}$		-0.15	-0.40
CI		$\text{AgCl} \rightarrow \text{Ag}$	$\text{AgBr} \rightarrow \text{Ag}$
AII	$\text{Ag} \rightarrow \text{AgO}^-$	$\text{Ag} \rightarrow \text{AgCl}_{n+1}^{n-}$	$\text{Ag} \rightarrow \text{AgBr}_{n+1}^{n-}$
$U^0, \text{V}_{\text{MSE}}$	-0.19	-0.19	-0.19
CII	$\text{AgO}^- \rightarrow \text{Ag}$	$\text{AgCl}_{n+1}^{n-} \rightarrow \text{Ag}$	$\text{AgBr}_{n+1}^{n-} \rightarrow \text{Ag}$
AIII	$\text{Ag} \rightarrow \text{AgOH} \rightarrow (\text{Ag}_2\text{O})$	$\text{Ag} \rightarrow \text{AgOH} \rightarrow (\text{Ag}_2\text{O})$	$\text{Ag} \rightarrow \text{AgOH} \rightarrow (\text{Ag}_2\text{O})$
$U^0, \text{V}_{\text{MSE}}$	-0.16	-0.16	-0.16
CIII	$(\text{Ag}_2\text{O}) \rightarrow \text{AgOH} \rightarrow \text{Ag}$	$(\text{Ag}_2\text{O}) \rightarrow \text{AgOH} \rightarrow \text{Ag}$	$(\text{Ag}_2\text{O}) \rightarrow \text{AgOH} \rightarrow \text{Ag}$

**TABLE 2: Charge and Quartz Microbalance Mass Change Data<sup>3</sup>**

reaction	$U, \text{V}_{\text{MSE}}$	$r_q, \%$		$r_m - r_q, \%$
		$\frac{ q^+  -  q^- }{ q^+ }$	$\frac{ \Delta m^+  -  \Delta m^- }{ \Delta m^+ }$	
$\text{Ag}/\text{AgI}$	-0.62	2	17	15
$\text{Ag}/\text{AgBr}$	-0.40	6	20	14
$\text{Ag}/\text{AgCl}$	-0.15	19	45	26
$(\text{Ag}/\text{AgX}_{n+1}^{n-})$	(-0.19)			
$(\text{Ag}/\text{Ag}_2\text{O})$	(-0.16)			

mass changes ( $\Delta f$ ) are negligible because dissolution and phase formation obviously counteracted in this potential range. Only after scan reversal at  $-0.1 \text{ V}_{\text{MSE}}$ , a frequency reduction of  $\Delta f \approx 10 \text{ Hz}$  indicated a mass gain of about 75 ng due to oxide nucleation partly compensated by dissolution mass losses. After passage through CIII and CII, the mass did not completely return to the original value ( $r_m \approx 20\%$ , Table 2), suggesting that either not all oxide could be reduced or/and  $\text{AgO}^-$  accumulated in the solution from other oxidation cycles led to mass increase by silver deposition. A further contribution to  $r_m$  may be an irreversible roughness increase ( $\Delta m_r$ ).<sup>39</sup> A 1D SFM topography-potential experiment gave support to this.<sup>40</sup> It could be shown that an anodic potential pulse triggered the dissolution to  $\text{AgO}^-$  and the formation of  $\text{Ag}_2\text{O}$ . After returning to a negative potential, both roughnesses on each single grain due to material removal, local  $\text{Ag}_2\text{O}$  or redeposited Ag features irreversibly remained on the surface. That means that Ag material has been dissolved as  $\text{AgO}^-$  into the electrolyte, while Ag tended to be converted to insoluble  $\text{Ag}_2\text{O}$  phases or Ag deposits near grain boundaries.

**3.3. Specific Halogenide Adsorption.** Addition of iodide and bromide led to the appearance of new peaks due to the  $\text{AgX}$  phase formation (AI) and  $\text{AgX}$  phase reduction (CI) near the potentials  $U_{\text{Ag}/\text{AgI}}^0 \approx -0.62 \text{ V}_{\text{MSE}}$  and  $U_{\text{Ag}/\text{AgBr}}^0 \approx -0.40 \text{ V}_{\text{MSE}}$ , respectively (Tables 1 and 2).<sup>3</sup> Specific adsorption of  $\text{X}^-$  at potentials negative of the respective  $U_{\text{Ag}/\text{AgX}}^0$  could be observed both by extremely sensitive EQMB measurements and by LFM. Current and frequency data for the KBr system are given in Figure 1b,d. Specifically adsorbed halogenide ( $\text{X}^-$ ) causes overall mass changes  $\Delta m$  according to

$$\Delta m \approx (\Gamma_X^I m_X^I + \Gamma_{CX}^I m_{CX}^I) A \quad (4)$$

Either partly solvated halogenide,  $\Gamma_X^I m_X^I$ , or halogenide paired with a cation (C),  $\Gamma_{CX}^I m_{CX}^I$ , contribute to the mass loading of the inner Helmholtz layer.  $\text{X}^-$  can compensate the metal charge; however, the neutral CX cannot contribute as counterion, and other anions like  $\text{F}^-$  are required in the outer Helmholtz layer. *Ex-situ* X-ray photoelectron spectroscopic measurements showed

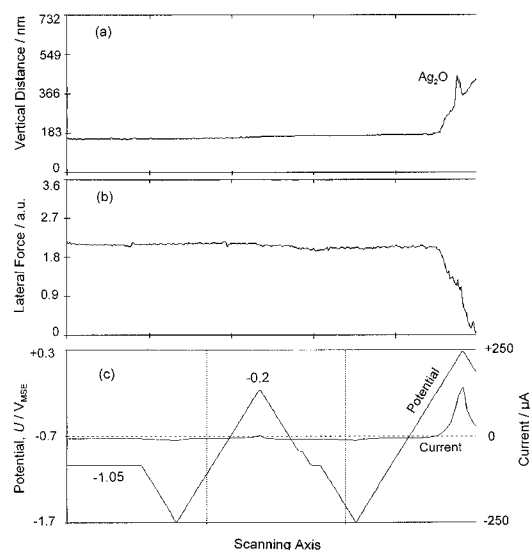


**Figure 2.** *In-situ* 1D topography/lateral force-potential sweep line scan of Ag in KF electrolyte (0.1 M KF, 0.01 M NaOH). 0.05 V s<sup>-1</sup>; (a) topographical line scan; (b) lateral force line scan; (c) electrode potential scan and current.

that in the case of Cl<sup>-</sup> adsorption Na<sup>+</sup>-Cl<sup>-</sup> ion couples are bound to a negatively charged surface even 0.4 V negative of the pzc, which is observed without specific adsorption ( $U_A^{q=0} \approx -0.7$  V<sub>MSE</sub>).<sup>4</sup> Actually, a maximum frequency and a minimum mass loading occurred around  $U_X^{q=0} \approx -1.0$  V<sub>MSE</sub> in the presence of Cl<sup>-</sup> and Br<sup>-</sup>. This is  $\sim 0.3$  V negative of  $U_A^{q=0} \approx -0.7$  V<sub>MSE</sub> without specifically adsorbed anions (e.g., Figure 1 in ref 3). That means that the pzc has been shifted from  $U_A^{q=0} \approx -0.7$  V<sub>MSE</sub> to  $U_X^{q=0} \approx -1.0$  V<sub>MSE</sub> in the presence of specifically adsorbed CX (e.g., K<sup>+</sup>-Cl<sup>-</sup>) pairs. In the range between  $-0.7$  and  $-1.0$  V<sub>MSE</sub>, the mass increase of cations in ion pairs,  $\Gamma_{CX}^I m_{CX}^I$ , compensated for the loss of solvated cations,  $\Gamma_C^O m_C^O$ , and little mass changes could be observed.<sup>3</sup> Positive of  $U_A^{q=0}$ , up to  $U_{Ag/AgX}^0$  (the formation potential of bulk conversion), the frequency decreased by 2.5 Hz. This corresponds to 28 ng on 0.28 cm<sup>2</sup> or a complete K<sup>+</sup>-Cl<sup>-</sup> monolayer to a first order approximation.

SFM of specifically bound halogenides on silver has been unsuccessful up to now.<sup>5</sup> Atomic resolution observable at  $U < U_X^{q=0}$  changed to blurred images in the specific adsorption range. We therefore applied *in-situ* lateral force microscopy (LFM) to test the friction changes due to potential controlled chemical modification. We employed a one-dimensional (1D) LFM mode where the cantilever is only scanned back and forth on one defined line on the surface. As the second dimension of the LFM image, time or potential was chosen. Thus, time or potential resolved friction data could be achieved.

Figure 2 shows the changes of topography (a) and friction (lateral force microscopy, LFM) (b) at one particular point (extracted from the 1D LFM line scan) of the Ag surface in contact with an alkaline KF electrolyte (0.1 M KF, 0.01 M NaOH) which contains ions which maintain their solvation shell and do not undergo specific adsorption. Potential cycling (Figure 2c) around the pzc of  $U_A^{q=0} -0.7$  V<sub>MSE</sub> in the range between  $-1.7$  and  $U < U_{Ag/Ag_2O}^{q=0} = -0.16$  V<sub>MSE</sub> resulted in negligible morphological and frictional changes. No correlation between lateral force and charging of the electrochemical double layer is observable in this electrolyte. Only when potentials positive of  $U_{Ag/Ag_2O}^{q=0}$  were reached (see second anodic potential excursion), the growth of an oxide phase is registered morpho-

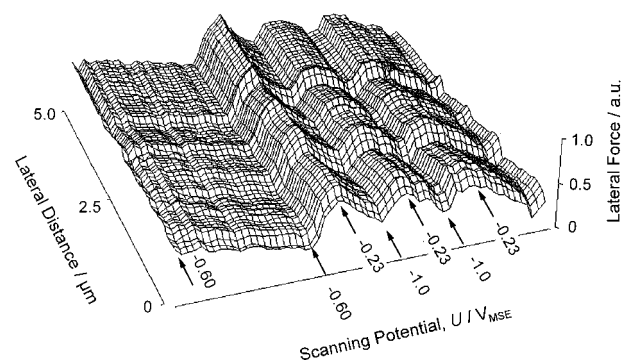


**Figure 3.** Specific adsorption of bromide. *In-situ* 1D lateral force-potential sweep image of Ag in KBr electrolyte (0.1 M KF, 0.01 M NaOH, 0.001 KBr). 0.05 V s<sup>-1</sup>. Reversal potentials of linear scans are indicated.

logically (Figure 2a) and by an anodic current peak (Figure 2c) accompanied by a drastic decrease of the lateral force data (Figure 2b).

Completely different LFM results were achieved after addition of anions which undergo specific adsorption while loosing part of their solvation shell. Actually, friction increased in the potential region positive of the pzc with X<sup>-</sup> present,  $U_X^{q=0} \approx -1.0$  V<sub>MSE</sub>, and negative of the oxide phase formation,  $U_{Ag/Ag_2O}^{q=0} = -0.16$  V<sub>MSE</sub>. Figure 3 shows a representative LFM-potential image with three potential cycles in the range between  $-1.0$  and  $-0.23$  V<sub>MSE</sub>. The friction changes were reversible, i.e., low friction was observed after cathodic desorption of Br<sup>-</sup> or K<sup>+</sup>-Br<sup>-</sup> ion couples, respectively. That suggests that *in-situ* LFM can be employed to monitor specific adsorption and, more generally, chemical conversion reactions in submonolayers of atomic species which are inaccessible to topological imaging by SFM.

The enhancement of friction by specific adsorption may be due to either changes of the molecular roughness and chemical activity of the surface or the increase of the vertical force. Structure reorganizations of the electrochemical double layer during specific adsorption suggest substantial tribological and rheological changes. Hydrated anions (e.g., F<sub>aq</sub><sup>-</sup>) adsorbed in the outer Helmholtz plain are not locally bound to a specific site but only electrostatically attracted by a delocalized countercharge under the surface of the electronic conductor electrode. Thus, they can be shifted sideways by the lateral movement of the cantilever so that friction is comparatively low (Figure 4a). Specific adsorption of an anion, on the other hand, takes place by a chemical bond to a specific surface site (atom), and lateral movement is impeded resulting in higher friction (Figure 4b). Water dipole density changes<sup>22</sup> are only related to the charging of the interface and are not directly related to the occurrence of specific surface bonds and therefore give negligible contributions to this phenomenon. The charging state of the insulating cantilever surface (Si<sub>3</sub>N<sub>4</sub>) is most probably constant, but unknown in sign and value. The counterpart, i.e., the silver surface, changes charge according to the potential applied. Thus, vertical force and, as a consequence, friction force could change depending on the dielectric shielding of species present (ionic strength etc.) when the fixed cantilever surface charges replace counterions in the outer Helmholtz plain. The presence of specifically adsorbed ion pairs does not contribute to the double layer charging. Actually, LFM results in the presence of KF (Figure 2) proved that electrostatic force changes between cantilever and electrode surface as reason for the observed frictional increase are negligible. That also indicates that the electrochemical double layer (inner and outer Helmholtz plain)

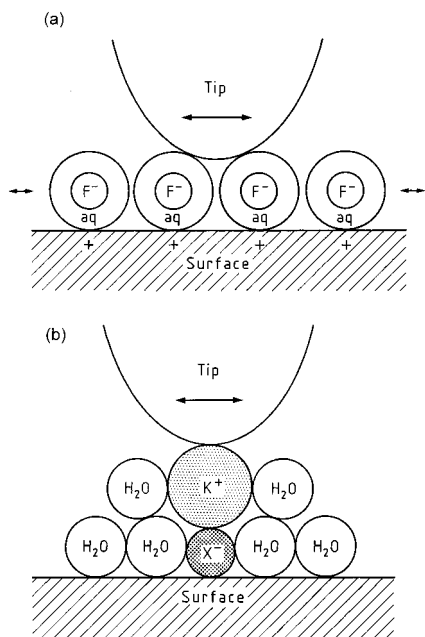


**Figure 4.** Nanotribological model for the double layer potential region: (a) electrostatically attracted and laterally mobile solvated anions ( $F^-$ ); (b) specifically adsorbed (locally chemisorbed) and immobilized anions  $X^-$  (e.g.,  $I^-$ ,  $Br^-$ ,  $Cl^-$ ) as ion pair with a cation ( $K^+$ ).

stays intact underneath the cantilever tip at comparatively high ionic strength in the electrolyte.

**3.4. Formation of AgI and AgBr Phases.** The formation of bulk silver halogenide on the electrode starts at the respective potential  $U_{Ag/AgX}^{q=0}$ . Analogous EQMB results were found with iodide and bromide. When AI starts evolving at, e.g.,  $U_{Ag/AgBr}^{q=0}$  (Figure 1b), the frequency commences to reduce steeply (Figure 1d). After passage through the dissolution potential  $U_{Ag/AgBr}^{n-} \approx -0.19 V_{MSE}$  and the corresponding anodic wave AII, the slope of  $\Delta f$  is reduced to some extent. That means that dissolution mass losses counteract the mass gain of the AgBr formation. Oxide formation (AIII) is only a minor contribution ( $\sim 10\%$ ) according to the current and mass data of the KF solution (Figure 1a,c). Once  $AgBr_{n-}^{n-}$  reduction and redeposition currents have ceased after passage through CII,  $\Delta f$  reached about 100 Hz (near  $U_{Ag/AgBr}^{q=0}$ ) corresponding to the entire AgBr mass formed. Scanning past CI increased  $\Delta f$ . However, a remnant mass ( $r_m \approx 20\%$ , Table 2) was observed. The charge balance  $r_q \approx 6\%$  (Table 2) is almost negligible; i.e., practically all AgBr has been reduced. Therefore,  $r_m$  has to be associated with Ag deposition from soluble  $AgBr_{n-}^{n-}$  species from the electrolyte bulk which were "lost" in previous anodic scans in the dissolution potential range. In the case of an iodide solution, one observed an analogous mechanism (Table 2). Spurious mass changes due to varying roughness ( $\Delta m_r$ ), or due to viscosity wall effects ( $\Delta m_\delta$ ), cannot be excluded without a microscopic *in-situ* technique. Normally, coverages from charge or mass data are always derived with the assumption of homogenous coverages. Conventional voltammetry but also EQMB  $\Delta f$  data cannot give any information about the homogeneity of surface reactions.

Therefore, *in-situ* SFM and LFM were used to resolve the open question of roughness and homogeneity. A long-range 2D SFM image of a silver surface in KF/KBr contact with the dimension  $2 \mu m \times 2 \mu m$  showed grains of the order of 100 nm and an absolute roughness of the order of 50 nm (Figure 5). Potential pulses from  $-1.0 V_{MSE}$  into the region of AgBr formation, i.e., to  $U = -0.3 V_{MSE}$  ( $> U_{Ag/AgBr}^0 \approx -0.40 V_{MSE}$ ), generated inhomogeneously distributed smooth islands inde-

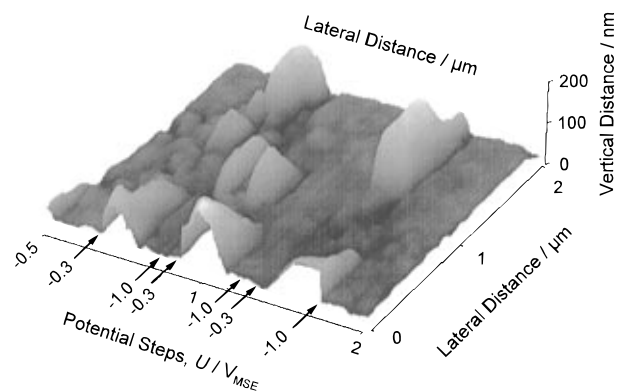


**Figure 5.** *In-situ* 2D topographical scanning force-potential step image of Ag in KBr electrolyte (0.1 M KF, 0.01 M NaOH, 0.001 KBr). Potential steps are indicated (sweep left to right).

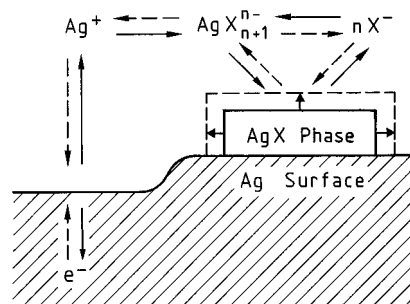


**Figure 6.** Dissolution-precipitation mechanism of the electrochemical silver halogenide (AgX) phase formation and dissolution:—anodic reaction, --- cathodic process.

pendent of epitaxial information. They were almost an order of magnitude wider than the average grain size of the Ag substrate and attained heights of the order of 100–200 nm. Obviously, this phase formation took place according to a dissolution-precipitation mechanism (Figure 6). The reductive potential pulses ( $\sim -1.0 V_{MSE}$ ) resulted in the complete removal of the AgBr bodies (Figure 5), which is typical for this mechanism.

Repetition of such an electrochemical manipulation resulted in new irreversible deposits appearing preferentially along surface steps (not shown here). These irreversible features were Ag deposits generated during redeposition of soluble  $AgBr_{n-}^{n-}$  species (CII, Figure 1b; Figure 6). This finding supports the above hypothesis that the discrepancy between anodic and cathodic mass changes (Table 2) is mainly due to Ag deposits. This type of extremely inhomogeneously distributed features may contribute to roughness frequency artifacts ( $\Delta m_r$ ) only to a negligible extent.

**3.5. Formation of AgCl Phases.** The formation of AgCl in the presence of  $Cl^-$  ions runs under very different conditions as compared to AgI and AgBr. It cannot be resolved by voltammetry as an AI type peak, because  $U_{Ag/AgCl}^0$  is near the potential of the chloride accelerated dissolution (AII)  $U_{Ag/AgCl}^{n-}$  and near  $U_{Ag/Ag_2O}^0$  of the oxide formation (AIII) (Table 1, compare also refs 3 and 40). Thermodynamics suggest that the dissolution reaction to  $AgCl_{n-}^{n-}$  should set in more negatively than both conversion reactions. The combination of the reduction voltammogram and the EQMB mass data (Figure 2 in ref 3), however, allowed the separation of these three reactions. Typical for the AgCl system is the negatively separated strong reduction current of the soluble Ag species (CII; ref 3) in contrast to, e.g., CII of the AgBr system (Figure 1b). Upon potential scan reversal, first AgCl (and any oxide if present) is stripped (CI + CIII) followed by the redeposition

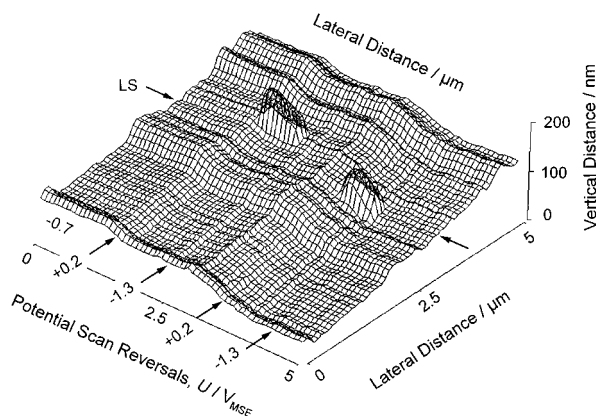


**Figure 7.** *In-situ* 1D topographical scanning force–potential sweep image of Ag in KCl electrolyte (0.1 M KF, 0.01 M NaOH, 0.001 M KCl). Reversal potentials of linear scans are indicated. LS: line scan depicted explicitly in Figure 8.

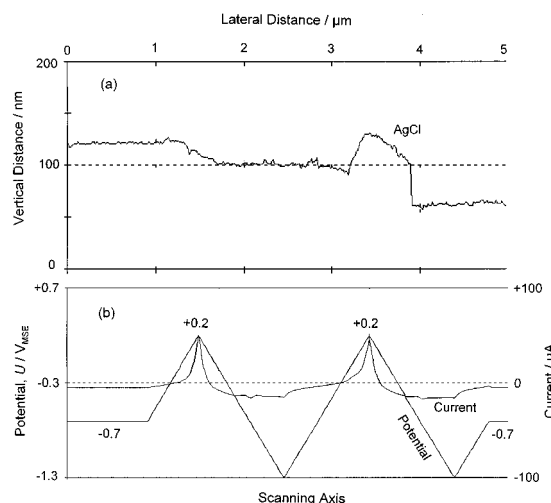


**Figure 8.** *In-situ* 1D topography–potential sweep line scan of Ag in KCl electrolyte (0.1 M KF, 0.01 M NaOH).  $0.05 \text{ V s}^{-1}$ ; (a) topographical line scan; (b) electrode potential scan and current.

of Ag from soluble  $\text{AgCl}_{n+1}^{n-}$  at  $U < U_{\text{Ag}/\text{AgCl}_{n+1}}^0$  (CII). Charge measurements in the AgCl system resulted in unresolved discrepancies of the anodic and cathodic values ( $r_q$ ) (Table 2); i.e., the anodic charge is by  $\sim 20\%$  greater than could be “harvested” during the cathodic scan. Obviously, a substantial amount of oxidative products like  $\text{AgCl}_{n+1}^{n-}$  have been lost into the electrolyte volume. This is supported by a potentiodynamic 1D topographical SFM (Figure 7). Figure 8 gives a profile trace along the line indicated in Figure 7. Potentials between  $\sim -0.2 \text{ V}_{\text{MSE}}$  and  $U_{\text{Ag}/\text{AgCl}}^0 \approx -0.15 \text{ V}_{\text{MSE}}$  did not lead to conversion to AgCl but to substantial dissolution ( $\sim 50 \text{ nm}$  per cycle) and remarkable smoothening ( $< 10 \text{ nm}$ ). This electropolishing practically removed the grain topography. That means that EQMB mass measurements were not affected by any roughness increase ( $\Delta m_r \approx 0$ ). Near  $U_{\text{Ag}/\text{AgCl}}^0$ , a complicated situation occurred; i.e., AgCl phase formation is accompanied by dissolution. More than 50-nm-high relatively smooth islands are deposited which resemble the AgBr features described above. Negative scanning removed them completely. Interestingly, growth sites changed with each cycle (Figure 7), indicating characteristics of a dissolution–precipitation mechanism in analogy to the  $\text{Br}^-$  and  $\text{I}^-$  systems (Figure 6).

#### 4. Conclusions

(1) Specific adsorption of  $\text{X}^-$  at potentials negative of the respective silver halogenide phase formation potential

$U_{\text{Ag}/\text{AgX}}^0$  could be observed both by extremely sensitive electrochemical quartz microbalance measurements (EQMB) and by *in-situ* lateral force microscopy (LFM).

(2) *In-situ* LFM can exploit nanotribological changes to monitor specific adsorption and, more generally, chemical conversion reactions in submonolayers of atomic species which are inaccessible to topological imaging by scanning force microscopy (SFM).

(3) Positive of the point of zero charge, e.g.,  $U_{\text{X}}^{q=0} \approx -1.0 \text{ V}_{\text{MSE}}$ , up to the silver halogenide formation potential  $U_{\text{Ag}/\text{AgX}}^0$ , the EQMB frequency decrease corresponds to the formation of approximately one monolayer of specifically adsorbed cation halogenide ion pairs.

(4) Reorganization of the electrochemical double layer during specific adsorption in the potential range  $U_{\text{X}}^{q=0} < U < U_{\text{Ag}/\text{AgX}}^0$  causes nanotribological changes. Hydrated anions in the outer Helmholtz plain are not locally bound to a specific site and can be shifted sideways by the motion of the cantilever. Thus, LFM shows no friction changes (Figure 2). Specific adsorption of an anion, on the other hand, is connected with a chemical bond to a specific surface site. Thus, lateral translation is impeded, resulting in increased friction (Figure 3).

(5) The electrochemical double layer (inner and outer Helmholtz plain) stays intact underneath the cantilever tip at comparatively high ionic strengths (0.1 M) in the electrolyte.

(6) Anodic dissolution of silver to  $\text{AgO}^-$  and the formation of  $\text{Ag}_2\text{O}$  islands in a halogenide-free alkaline solution contribute to a general roughening of the surface. Corrosion results in pits and terraces on the silver grains. Anodically formed  $\text{Ag}_2\text{O}$  and cathodically deposited silver phases correspond to the substrate morphology and grow on grain boundary sites.

(7) *In-situ* SFM showed that silver halogenide phases are anodically nonuniformly formed as smooth islands which are much larger (diameter  $\leq 1 \mu\text{m}$ , height  $\leq 200 \text{ nm}$ ) than the underlying metal grains (100–200 nm) and are located in no observable correspondence to grain surfaces or boundaries. Since these island features grow on the metal surface already covered by a specifically adsorbed halogenide film, this behavior suggests a dissolution–precipitation growth analogous to a Stranski–Krastanov mechanism.

(8) Silver iodide and bromide phases can almost reversibly be reduced. Irreversible mass gains after an oxidation reduction cycle can be associated with Ag deposition near surface steps ( $\leq 50 \text{ nm}$  high) from soluble  $\text{AgI}_{n+1}^{n-}$  and  $\text{AgBr}_{n+1}^{n-}$  species which were “lost” in the electrolyte bulk during previous anodic scans in the dissolution potential range.

(9) Anodic AgCl formation runs under very different conditions than that of AgI and AgBr. At least two processes occur concurrently: the silver surface is vigorously electropolished and soluble  $\text{AgCl}_{n+1}^{n-}$  species evolve, while AgCl islands precipitate on the newly generated surface regardless of the original grain topography.

(10) AgCl can be completely reduced according to the dissolution–precipitation mechanism. The charge and the EQMB mass balance suggest that more dissolved  $\text{AgCl}_{n+1}^{n-}$  is “harvested” as silver deposits than has been dissolved in one anodic cycle only.

#### References and Notes

- (1) Hamelin, A.; Vitanov, T.; Sevestyanov, E.; Popov, A. *J. Electrochem. Soc.* **1983**, *145*, 225.
- (2) Weaver, M. J.; Hupp, J. T.; Barz, F.; Gordon, J. G., II; Philpott, M. R. *J. Electroanal. Chem.* **1984**, *460*, 321.
- (3) Kautek, W.; Sahre, M. in *Elektrochemie und Werkstoffe*; GDCh-Monographie; Gesellschaft Deutscher Chemiker: Frankfurt am Main, 1995; Vol. 2, p 359.

- (4) Kautek, W.; Gordon, J. G., II *J. Electrochem. Soc.* **1990**, *137*, 3405.
- (5) Sneddon, D. D.; Sabel, D. M.; Gewirth, A. A. *J. Electrochem. Soc.* **1995**, *142*, 3027.
- (6) *Surface Enhanced Raman Scattering*; Chang R. K., Furtak, T. E., Eds., Plenum Press: New York, 1982.
- (7) Kanazawa, K. K.; Gordon, J. G., II *Anal. Chim. Acta* **1985**, *175*, 99.
- (8) (a) Bruckenstein, S.; Shay, M. *J. Electroanal. Chem.* **1985**, *188*, 131. (b) Bruckenstein, S.; Shay, M. *Electrochim. Acta* **1985**, *30*, 1295.
- (9) Benje, M.; Eiermann, M.; Pittermann, U.; Weil, K. G. *Ber. Bunsenges. Phys. Chem.* **1986**, *90*, 435.
- (10) (a) Buttry, D. A. In *Electroanalytical Chemistry*, Bard, A. J., Ed.; Marcel Dekker Inc.: New York, 1991; Vol. 17, p 1. (b) Buttry, D. A. In *Electrochemical Interfaces: Modern Techniques for in-situ Interface Characterization*; Abruna, H. D., Ed.; Verlag Chemie: Weinheim, 1991; p 529. (c) Buttry, D. A.; Ward, M. D. *Chem. Rev.* **1992**, *92*, 1355.
- (11) Kautek, W.; Sahre, M.; Soares, D. M. *Ber. Bunsenges. Phys. Chem.* **1995**, *99*, 667.
- (12) Lee, W.-W.; White, H. S.; Bard, M. D. *Anal. Chem.* **1993**, *65*, 3232.
- (13) Soares, D. M.; Kautek, W.; Fruböse, C.; Doblhofer, K. *Ber. Bunsenges. Phys. Chem.* **1994**, *98*, 219.
- (14) Tsionsky, V.; Daikhin, L.; Gileadi, E. *J. Electrochem. Soc.* **1996**, *143*, 2240.
- (15) Yang, M.; Thompson, M.; Duncan-Hewitt, W. C. *Langmuir* **1993**, *9*, 802.
- (16) Beck, R.; Pittermann, U.; Weil, K. G. *J. Electrochem. Soc.* **1992**, *139*, 453.
- (17) Urbakh, M.; Daikhin, L. *Langmuir* **1994**, *10*, 2836.
- (18) Kautek, W.; Sahre, M. *Surf. Coatings Technol.* **1994**, *67*, 167.
- (19) Robbin, M. O.; Thompson, P. A.; Grest, G. S. *MRS Bull.* **1993**, *18*, 45.
- (20) Raghavan, K.; Foster, K.; Motakabbir, K.; Berkowitz, M. *J. Chem. Phys.* **1991**, *94*, 2110.
- (21) Russell, A. E.; Lin, A. S.; O'Grady, W. E. *J. Chem. Soc. Faraday Trans.* **1993**, *89*, 195.
- (22) Toney, M. F.; Howard, J. N.; Richer, J.; Borges, G. L.; Gordon, J. G., II; Melroy, O. R.; Wiesler, D. G.; Yee, D.; Sorensen, L. B. *Nature* **1994**, *368*, 444.
- (23) Exner, A. M. In *Materials Science and Technology*; Verlag Chemie: Weinheim, New York, 1994; Vol. 2B, p 281.
- (24) DiNardo, N. J. *Nanoscale Characterization of Surfaces and Interfaces*; Verlag Chemie: Weinheim, New York, 1995.
- (25) Kautek, W. *Corrosion Sci.* **1988**, *28*, 173.
- (26) Gewirth, A. A.; Hanson, K. J. *Interface* **1993**, *2*, Spring, 37.
- (27) Soares, D. M. *Meas. Sci. Technol.* **1993**, *4*, 549.
- (28) Perkins, R. S.; Andersen, T. N. In *Modern Aspects of Electrochemistry*; Butterworths: London, 1969; Vol. 5, p 203.
- (29) Valette, G.; Hamelin, A. *J. Electroanal. Chem.* **1973**, *45*, 301.
- (30) Zeelinskii, A. G.; Beck, R. Yu. *Sov. Electrochem.* **1978**, *14*, 1583.
- (31) Bagotskaya, I. A.; Damaskin, B. B.; Levi, M. D. *J. Electroanal. Chem.* **1980**, *115*, 189.
- (32) Sevast'yanov, E. S.; Ter-Akopyan, M. N.; Chubarova, V. K. *Sov. Electrochem.* **1980**, *16*, 368.
- (33) Bockris, J. O'M.; Argade, S. D.; Gileadi, E. *Electrochim. Acta* **1969**, *14*, 1259.
- (34) Burstein, G. T.; Newman, R. C. *Electrochim. Acta* **1980**, *25*, 1009.
- (35) Trasatti, S. *J. Electroanal. Chem.* **1984**, *172*, 27.
- (36) Hamelin, A.; Vitanov, T.; Sevastianov, E.; Popov, A. *J. Electroanal. Chem.* **1983**, *145*, 225.
- (37) Vorotyntsev, M. A. In *Modern Aspects of Electrochemistry*; Bockris, J. O'M., Conway, B. E., White, R. E., Eds.; Plenum Press: New York, 1986; Vol. 17, p 131.
- (38) Poubaix, M. *Atlas d'équilibres électrochimiques à 25 °C*; Gauthier-Villars: Paris, 1963.
- (39) Schumacher, R.; Gordon, J. G., II; Melroy, O. *J. Electroanal. Chem.* **1987**, *216*, 127.
- (40) Kautek, W.; Dieluweit, S.; Sahre, S. *PTB-Bericht* **1995**, *F-21*, 121.